Boundary-Layer Meteorol (2012) 142:149–175
DOI 10.1007/s10546-011-9663-8

ARTICLE

Simulating Australian Urban Climate in a Mesoscale Atmospheric Numerical Model

Marcus Thatcher · Peter Hurley

Received: 21 December 2010 / Accepted: 6 October 2011 / Published online: 29 October 2011

Abstract We develop an urban canopy scheme coupled to a mesoscale atmospheric numerical model and evaluate the simulated climate of an Australian city. The urban canopy scheme is based on the Town Energy Budget approach, but is modified to efficiently represent the predominately suburban component of Australian cities in regional climate simulations. Energy conservation is improved by adding a simple model of air-conditioning to prevent the urban parametrization acting as an energy sink during the Australian summer. In-canyon vegetation for suburban areas is represented by a big-leaf model, but with a largely reduced set of prognostic variables compared to previous approaches. Although we have used a recirculation/venting based parametrization of in-canyon turbulent heat fluxes that employs two canyon wall energy budgets, we avoid using a fixed canyon orientation by averaging the canyon fluxes after integrating over 180° of possible canyon orientations. The urban canopy scheme is evaluated by simulating the climate for Melbourne, Australia after coupling it to The Air Pollution Model. The combined system was found to predict a realistic climatology of air temperatures and winds when compared with observations from Environmental Protection Authority monitoring stations. The model also produced a plausible partitioning of the urban energy budget when compared to urban flux-tower studies. Overall, the urban canyon parametrization appears to have reasonable potential for studying present and predicting changes in future Australian urban climates in regional climate simulations.

Keywords Mesoscale environmental modelling · Surface energy balance · Urban canopy model

1 Introduction

The ability to simulate the urban climate in mesoscale and local-scale atmospheric numerical models is becoming increasingly important for regional climate modelling. In particular, changes to urban climate under global warming scenarios can have significant implications

M. Thatcher (✉) · P. Hurley
CSIRO Marine and Atmospheric Research, Aspendale, Australia
e-mail: Marcus.Thatcher@csiro.au

for energy usage and network stability (Sailor 2001), air pollution and public health (Jacob and Winner 2009) and building infrastructure. Over recent years, there has been significant progress in the development of building-averaged urban canopy models (UCMs), which attempt to simulate the urban energy budget without the substantial computational requirements of a building-resolving urban simulation. UCMs coupled to regional atmospheric models can then potentially be used to investigate the dynamical behaviour of the urban climate under global warming scenarios, as well as explore the consequences of different strategies for urban design.

Urban canopy models were once based on slab models (Oke 1988), which basically describe the urban environment as a concrete plate with modified roughness length and thermal properties that are appropriate for simulating the urban energy budget. Subsequently, urban canyon models were developed (Masson 2000; Kanda et al. 2005; Harman and Belcher 2006) that separate the urban energy budget into budgets for roofs, roads and walls. Such models also include shadowing effects due to the canyon geometry and parametrize the in-canyon exchange of turbulent heat fluxes. Canyon models have been extended to multiple-level models in an attempt to resolve the vertical structure of the urban canopy layer (Kusaka et al. 2001; Martilli et al. 2002), used canyon geometries based on a three-dimensional array of blocks (Kanda et al. 2007) include vegetation within the canyon (Lee and Park 2008), and include waste heat due to air-conditioning (Ohashi et al. 2007). A common feature of many building-averaged UCMs is their reliance on Monin–Obukhov similarity theory (MOST) to couple the urban canopy to the atmosphere, which makes the urban schemes compatible with most mesoscale atmospheric models. A UCM that contains all of the essential urban physical parametrizations is the Town Energy Budget (TEB) model described in Masson (2000).

In this paper we develop a UCM to be used in regional climate models (RCMs) for simulating the present day and potentially future climate of Australian cities. In this context, the UCM is used to predict the climatology of Australian cities (e.g., probability distributions and seasonal variability) over prolonged time integrations from years to decades. Furthermore, the UCM needs to be robust against errors arising from the host atmospheric model fluxes as well as errors arising from feedbacks between the UCM and the atmosphere. The UCM used is based on the TEB one-dimensional canyon approach (Masson 2000), but includes three basic modifications for Australian regional climate simulations. The first modification is to include a parametrization of idealized air-conditioners, which prevents the UCM acting as an unphysical energy sink during the Australian summer. Waste heat from air-conditioning has been previously simulated by Ohashi et al. (2007), although we have chosen to use a simpler scheme since it avoids introducing additional prognostic variables into the UCM. The second modification is to include an efficient big-leaf model to represent in-canyon vegetation in the predominately suburban component of Australian cities. In-canyon vegetation has been previously investigated by Lee and Park (2008), who argued that a big-leaf model directly coupled to canyon energy budgets can improve the representation of urban surface temperatures and the partitioning of sensible and latent heat fluxes. Our UCM also parametrizes in-canyon vegetation using a big-leaf model, but with a largely reduced set of prognostic variables to improve the computational efficiency of the UCM. Canyon turbulent heat fluxes between walls, roads and in-canyon vegetation are parametrized according to Harman et al. (2004b) and Harman and Belcher (2006), which is based on the circulation of air within the canyon. However, this parametrization of turbulent heat fluxes utilizes two canyon wall energy budgets (i.e., for the recirculation and venting sides of the canyon), whereas the TEB model employs a single wall energy budget after integrating the canyon fluxes over 360° of possible canyon orientations. Instead of using a single fixed canyon orientation within a grid box, our third modification is to derive the two wall energy budgets by integrating the

canyon fluxes over 180° of possible canyon orientations. We can then separate the canyon wall energy budgets without needing to assign a preferential canyon orientation for each grid box (i.e., more consistent with the original TEB formulation). For completeness, the UCM does support a single level snow scheme [based on Douville et al. (1995)], but we have neglected the discussion of snow herein since it is not relevant for simulating the climate of most Australian cities. The parameters used to describe the UCM are constrained by measurements described in the literature, with the canyon geometry being determined from measurements documented by Coutts et al. (2007).

We evaluate the UCM for present day Australian regional climate simulations by coupling it to The Air Pollution Model (TAPM), described by Hurley et al. (2005). TAPM was used to host the UCM, since it includes prognostic equations for meteorology and is capable of dynamically downscaling coarse resolution atmospheric datasets [e.g., National Centers for Environmental Prediction (NCEP) 2.5° reanalyses] to a 3-km resolution using a multiple nesting technique. TAPM also includes air pollution modelling capabilities relevant to urban environments and can be operated over annual and decadal time scales within a practical amount of time (e.g., approximately six hours per simulation year on a 3 GHz Intel Core 2 Duo computer using a single processor). Since the accuracy of the simulated air pollution depends on the accuracy of the simulated meteorology, then we have decided to only evaluate the meteorological component of the model. Nevertheless, once the meteorological response to the UCM is evaluated, then the system could be used to investigate changes to air quality in future climate projections using TAPM's air pollution modelling capabilities. We evaluate the performance of the combined UCM and TAPM model using observations from three Environmental Protection Authority (EPA) monitoring sites located in Melbourne, Australia. The EPA monitoring sites are chosen to compare differences between coastal, inland, inner city and outer suburban locations. We also compare the partitioning of the urban energy budget with the flux-tower measurements described in Coutts et al. (2007), to determine whether the energy partitioning predicted by the model is plausible. For reference, the UCM is compared with TAPM's standard slab urban scheme to demonstrate some of the potential improvements.

Section 2 describes the urban canopy scheme used, while Sect. 3 provides a technical description of the atmospheric model TAPM and its coupling to the UCM. Section 4 explains the design of the urban climate experiments and the results that were obtained, while the results are then summarized in Sect. 5.

2 Description of the Urban Canyon Model

This section outlines the design of the UCM, which is based on the TEB approach, but includes modifications to efficiently represent suburban areas in regional climate simulations. We first summarize the energy and flux budgets that determine the behaviour of the UCM (Sect. 2.1) and then explain how these energy budgets are modified from the TEB approach when we propose parametrizations for air-conditioning (Sect. 2.2), in-canyon vegetation (Sect. 2.3) and for separating the energy budgets of the two canyon walls (Sect. 2.4). Parametrizations not discussed in this section (e.g., radiation, conduction and surface water), and a summary of the model parameters, are described in the Appendix.

2.1 Urban Energy and Flux Budgets

To parametrize the urban environment, most UCMs separate the urban energy budget into components for roofs, roads and walls. In the TEB model scheme, the canyon fluxes are

integrated over 360° to represent all possible canyon orientations within a grid box. This results in a single wall temperature being representative of the wall temperatures on both sides of the canyon. Empirical parametrizations of aerodynamic resistances are then used to calculate the sensible heat flux from canyon surfaces (e.g., Masson 2000; Kusaka et al. 2001). An alternative parametrization of in-canyon fluxes has been developed by Harman et al. (2004b), which is based on how air is recirculated and vented within the canyon. The scheme predicts changes in turbulent fluxes as a function of the canyon height-to-width ratio, h/w, and it is relatively straightforward to include in-canyon vegetation (see Sect. 2.3). The parametrization also predicts different fluxes for walls in the recirculation region compared to walls in the venting region, so that the approximation of a single canyon wall energy budget is no longer appropriate. To employ this recirculation/venting based parametrization of canyon turbulent heat fluxes in a UCM then requires a method for separating the canyon wall energy budget into two budgets for walls on either side of the canyon. We also wish to avoid a preferential canyon orientation within a grid box as the UCM is intended to represent a building averaged scale of the urban environment. To this end, we have integrated the canyon over 180° of possible orientations, which results in the separation of canyon walls with a component facing in the easterly direction and walls with a component facing in the westerly direction. The two canyon wall energy budgets are referred to as 'east' and 'west' (facing) walls in the discussion below. The energy budgets for canyon walls could have alternatively been separated into north facing walls and south facing walls when integrating the different canyon orientations through 180°. However, as discussed in Sect. 2.4, the diurnal temperature cycle averaged over all canyon walls shows two local maxima that correspond to the temperature maxima of east-facing walls and the temperature maxima of west-facing walls. Consequently we have chosen to separate the wall energy budgets into east and west facing walls so as to better represent the diurnal temperature cycle of canyon walls. The separation into east- and west-facing walls is also broadly consistent with Harman and Belcher (2006), where a single fixed north-south canyon orientation was used.

Following the TEB model, we divide the building materials into three layers, with the energy budget for the surface layer ($i = 1$) described by

$$C_{*,1}\frac{\mathrm{d}T_{*,1}}{\mathrm{d}t} = \frac{1}{d_{*,1}}\left(S_* + R_* - H_* - LE_* - G_{*,1}\right), \tag{1}$$

where $*$ can take the value of roof, road, east (wall) and west (wall), and $C_{*,1}$, $T_{*,1}$ and $d_{*,1}$ are the heat capacity, temperature and thickness of the top layer of the urban surface, respectively. For convenience, we use $T_* = T_{*,1}$ below as shorthand to represent the surface temperature of urban building materials. S_* is the net shortwave radiative flux, R_* is the net longwave radiative flux, H_* is the sensible heat flux, LE_* is the latent heat flux and $G_{*,1}$ is the heat conducted from the surface to an adjacent layer of the building material. As stated in the introduction, we neglect the energy budget for snow. The values for the parameters $C_{*,1}$ and $d_{*,1}$ depend on the materials used for building construction and are defined in the Appendix. The energy budget for the remaining two layers can be written as

$$C_{*,i}\frac{dT_{*,i}}{\mathrm{d}t} = \frac{\left(G_{*,i-1} - G_{*,i}\right)}{d_{*,i}}, \tag{2}$$

where $i = 2, 3$ is the 2nd and 3rd building material layer, respectively. We calculate $G_{*,i}$ using the same approach as described by Masson (2000) (see also the Appendix). Note that heat is transferred into the building interior ($G_{*,3} > 0$) when the temperature of the third building layer, $T_{*,3}$, is greater than the indoor comfort temperature, T_{bld}, whereas heat is removed from the building interior ($G_{*,3} < 0$) when $T_{*,3}$ is lower than T_{bld}.

As discussed in Sect. 1, the UCM includes in-canyon vegetation to represent suburban areas. The in-canyon vegetation requires an additional energy budget as described by

$$0 = S_{\text{vegt}} + R_{\text{vegt}} - H_{\text{vegt}} - LE_{\text{vegt}}, \tag{3}$$

where we follow Kowalczyk et al. (1994) and diagnose the vegetation canopy temperature, T_{vegt}, that satisfies the energy budget in Eq. 3. This differs from the approach described in Lee and Park (2008), where the canopy air temperature is a prognostic variable. Diagnosing the vegetation canopy temperature also ensures the scheme remains numerically stable with the relatively large timesteps that are typically used in regional climate simulations. The calculations of the fluxes for the in-canyon vegetation are discussed in Sect. 2.3.

The different components of the urban canyon (i.e., walls, roads and vegetation) are coupled in terms of radiation, the canyon sensible heat budget and the canyon latent heat budget. The canyon sensible and latent heat flux budgets can be written as

$$\begin{aligned} H_{\text{can}} = {} & (1 - \delta_{\text{vegt}})H_{\text{road}} + \delta_{\text{vegt}}H_{\text{vegt}} + (h/w)(H_{\text{east}} + H_{\text{west}}) \\ & + H_{\text{traf}} + H_{\text{AC}}, \end{aligned} \tag{4}$$

$$LE_{\text{can}} = (1 - \delta_{\text{vegt}})LE_{\text{road}} + \delta_{\text{vegt}}LE_{\text{vegt}}, \tag{5}$$

where H_{can} and LE_{can} describe the transfer of sensible and latent heat within the atmospheric model (i.e., leaving the canyon) and H_{traf} is the sensible heat flux due to traffic. Here, H_{traf} is estimated from January measurements made by Coutts et al. (2007) and is assumed to be a valid approximation for all seasons. We have also included a contribution due to air-conditioning, H_{AC}, which describes the transfer of heat from within the buildings into the canyon and is discussed in Sect. 2.2. Note that δ_{vegt} represents the portion of the canyon floor that is occupied by vegetation.

The output from the UCM to the host atmospheric model includes outgoing longwave radiation, R_{out}, sensible heat flux, H_{out} and latent heat flux, LE_{out}, which are defined as

$$R_{\text{out}} = \delta_{\text{bld}}R_{\text{roof}} + (1 - \delta_{\text{bld}})R_{\text{can}}, \tag{6}$$

$$H_{\text{out}} = \delta_{\text{bld}}H_{\text{roof}} + (1 - \delta_{\text{bld}})H_{\text{can}}, \tag{7}$$

$$LE_{\text{out}} = \delta_{\text{bld}}LE_{\text{roof}} + (1 - \delta_{\text{bld}})LE_{\text{can}}, \tag{8}$$

where R_{can} is the outgoing longwave radiative flux from the canyon (see Appendix) and δ_{bld} is the relative fraction of the urban area occupied by buildings. The sensible heat flux due to industry is set to zero for the results shown herein.

The solution to the energy budget and flux budget equations (Eqs. 1–5) is the basis of the UCM described. In this model, Eqs. 3–5 are each solved iteratively in terms of the vegetation canopy temperature, T_{vegt}, the canyon air temperature, T_{can}, and the canyon water vapour mixing ratio, q_{can}, respectively. There are a number of ways to solve these coupled equations, however we have decided to use nested sectant solvers for the canyon latent heat flux, sensible heat flux and in-canyon vegetation. Although slower than, say, a multi-variable Newton–Raphson approach, the use of the sectant solvers ensures that the numerical solution still robustly converges if changes are made to the in-canyon parametrizations (i.e., there is no need to modify the solver if the parametrizations change). For realistic applications, the urban scheme takes less than 5% of the running time compared to the atmospheric host model's vegetation canopy scheme and hence the use of the nested sectant solvers does not detract from the overall running time of the host atmospheric model.

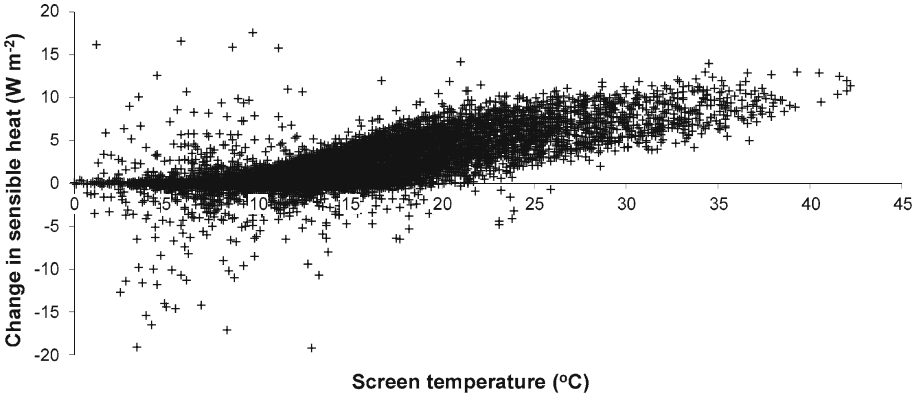

Fig. 1 Plot of the change in sensible heat flux between with and without air-conditioning parametrized in Eq. 9, as a function of the simulated screen temperature. The results are based on a year long simulation, described in Sect. 4. Model parameters were chosen to represent a generic Australian city (see Appendix)

2.2 Air-Conditioning

Since the UCM is intended for regional climate simulations with simulated time durations of years to decades, then we wish to conserve energy where appropriate in the urban energy budget. To this end, we assume that when the net heat flux $G_{*,3}$ is negative (i.e., heat leaving the room), then heating is supplied (e.g., burning fuel). However, when the net heat flux $G_{*,3}$ is positive (i.e., heat entering the room) then we simply assume air-conditioning will pump that heat back into the canyon according to

$$H_{\mathrm{AC}} = \Gamma_{\mathrm{AC}} \max\left[\frac{G_{\mathrm{roof},3}\delta_{\mathrm{bld}}}{1-\delta_{\mathrm{bld}}} + \frac{h}{w}(G_{\mathrm{east},3} + G_{\mathrm{west},3}), 0\right], \tag{9}$$

where the δ_{bld} terms ensure energy is conserved by accounting for the relative difference in area covered by buildings and the canyon. Γ_{AC} describes the efficiency of air-conditioning to remove the excess heat that is entering the building and is defined as simply set to

$$\Gamma_{\mathrm{AC}} = \max\left(1 + \frac{T_{\mathrm{can}} - T_{\mathrm{bld}}}{T_{\mathrm{bld}}}, 1\right). \tag{10}$$

Note that Eq. 10 assumes an idealized air-conditioning unit, whereas real air-conditioners are somewhat less efficient (e.g., potentially by a factor of 3). A more sophisticated method for modelling air-conditioning is described in Ohashi et al. (2007), where heat load from internal building activities, ventilation and solar insolation through windows is also accounted for. Nevertheless, the simple approach in Eqs. 9–10 ensures that the energy of the urban system is conserved when the air temperature is in excess of the indoor comfort temperature, T_{bld}, without requiring any additional prognostic variables. In this way, the UCM can generate heat (i.e., due to heating within the building), but cannot remove heat except by pumping this heat back into the urban canyon.

Figure 1 shows the change in the net sensible heat flux from the urban area after adding the air-conditioning parametrization, compared to the simulated screen temperature. The parameters for the UCM are chosen to describe a generic Australian city (see Appendix) and the simulation was performed for one year as described in Sect. 4. The air-conditioning parametrization can be seen to increase the sensible heat flux as the air temperature increases

above the indoor comfort temperature $T_{\mathrm{bld}} = 18°\mathrm{C}$. This additional heat flux H_{AC} would otherwise be unaccounted for in the UCM, and during summer months can be comparable in size to traffic or industrial sources of turbulent heat fluxes (e.g., see Sect. 2.4). Although important to ensure energy is correctly conserved by the UCM, the size of H_{AC} is generally too small to make a noticeable impact on the simulated air temperature for the suburban area simulated herein. However, when high density urban parameters are used (e.g., $h = 18\,\mathrm{m}$, $w = 9\,\mathrm{m}$, $\sigma_{\mathrm{vegt}} = 0.1$, $\sigma_{\mathrm{bld}} = 0.65$), the inclusion of air-conditioning can modify the screen air temperature by up to 1.5°C, which is broadly consistent with the results of Ohashi et al. (2007).

2.3 In-Canyon Vegetation

Australian cities have a sizable suburban component, where the modelling of in-canyon vegetation is important. Some urban models have attempted to include the vegetation component by linearly combining fluxes from a vegetation canopy model and from an urban canopy model (i.e., a horizontal tiling approach). However, Lee and Park (2008) argued that coupling the vegetation within the canyon using a big leaf model could improve the prediction of surface temperatures and the partitioning of sensible and latent heat fluxes. In this section we propose an alternative scheme for representing in-canyon vegetation based on the big-leaf model described by Kowalczyk et al. (1994), but with simplifications to reduce the number of prognostic variables. In our parametrization, the vegetation canopy temperature, T_{vegt} is solved iteratively from the vegetation energy budget Eq. 3, whereas the canopy temperature is a prognostic variable in Lee and Park (2008). We also avoid the need to simulate multiple soil levels by assuming no bare ground within the canyon (see below). In this way, the parametrization of in-canyon vegetation is then designed to be reasonably efficient, while still simulating realistic fluxes within the urban canyon. Modifications to the albedo and emissivity of the canyon floor due to in-canyon vegetation are discussed in the Appendix. Sensible and latent heat fluxes for in-canyon vegetation are calculated using

$$H_{\mathrm{vegt}} = \rho_{\mathrm{a}} C_{\mathrm{a}} \left(T_{\mathrm{vegt}} - T_{\mathrm{can}}\right) / \Omega_{\mathrm{vegt}}, \tag{11}$$

$$LE_{\mathrm{vegt}} = w_{\mathrm{vegt}} \rho_{\mathrm{a}} L_{\mathrm{v}} \left(\mathrm{qsat}_{\mathrm{vegt}} - q_{\mathrm{can}}\right) / \Omega_{\mathrm{vegt}} + (1 - w_{\mathrm{vegt}}) P_{\mathrm{vegt}}, \tag{12}$$

where ρ_{a} is the density of air, C_{a} is the heat capacity of air and Ω_{vegt} is the aerodynamic resistance for vegetation described in Sect. 2.4, w_{vegt} indicates the fraction of leaves covered by water (see below), L_{v} is the latent heat of vaporization and $\mathrm{qsat}_{\mathrm{vegt}}$ is the saturated mixing ratio for in-canyon vegetation. Transpiration from in-canyon vegetation, P_{vegt}, is parametrized using the expression from Kowalczyk et al. (1994)

$$P_{\mathrm{vegt}} = \rho_{\mathrm{a}} L_{\mathrm{v}} \left(\mathrm{qsat}_{\mathrm{vegt}} - q_{\mathrm{can}}\right) / (\Omega_{\mathrm{vegt}} + \Delta\Omega_{\mathrm{vegt}}). \tag{13}$$

Note that max P_{vegt} is constrained by the amount of available soil moisture, m_{soil} (see below). The modification of the aerodynamic resistance for transpiration is defined as

$$\Delta\Omega_{\mathrm{vegt}} = \frac{230}{LAI} \frac{f_1 f_2}{f_3 f_4}, \tag{14}$$

where f_1, f_2, f_3 and f_4 are defined by Kowalczyk et al. (1994)

$$f_1 = (f + 1)/(f + 23/500), \tag{15}$$

$$f_2 = 0.5(m_{\mathrm{sfc}} - m_{\mathrm{wilt}})/(m_{\mathrm{soil}} - m_{\mathrm{wilt}}), \tag{16}$$

$$f_3 = 1 - 0.00025(\mathrm{qsat}_{\mathrm{vegt}} - q_{\mathrm{can}}) p_{\mathrm{surf}}/0.622, \tag{17}$$

$$f_4 = 1 - 0.0016(298 - T_{\text{can}})^2, \tag{18}$$

$$f = 1.1 S_{\text{vegt}}/(150 LAI), \tag{19}$$

and where LAI is the leaf area index, m_{sfc} is the soil field capacity, m_{wilt} is the wilting point and p_{surf} is the surface atmospheric pressure.

Note that models of the vegetative canopy usually simulate the soil temperature and moisture over multiple layers of varying depth. However, for our UCM we attempt to simplify the in-canyon vegetation by assuming that the outgoing longwave radiation from the vegetation tile is dominated by the vegetation canopy temperature T_{vegt} so that we can neglect the calculation of soil temperature. In the context of the big-leaf model described by Kowalczyk et al. (1994), we have effectively set the vegetation cover over soil to 100%. We also simplify the soil moisture to a simple bucket model instead of using multiple soil levels. This is feasible since there is no soil evaporation in our model (i.e., since the vegetation cover is 100%) and soil moisture is only lost by transpiration. We then define the change in soil moisture as

$$\frac{\mathrm{d}m_{\text{soil}}}{\mathrm{d}t} = \frac{c_1 Rnd_- - P_{\text{vegt}}/L_{\text{v}}}{\rho_w d_{\text{soil}}}, \tag{20}$$

where c_1 is a constant that depends on the soil texture, Rnd_- is the rainfall minus the component intercepted by the vegetative canopy, d_{soil} is the depth of the soil and ρ_w is the density of water. Water in excess of the soil saturated field capacity is fed back to the host model as runoff, so that the total water is conserved in the simulation. The budget for water on the vegetation canopy is calculated from

$$\frac{\mathrm{d}W_{\text{leaf}}}{\mathrm{d}t} = Rnd - \frac{w_{\text{vegt}} \rho_{\text{a}} \left(\text{qsat}_{\text{vegt}} - q_{\text{can}} \right)}{\Omega_{\text{vegt}}}, \tag{21}$$

where the maximum value of W_{leaf} is limited to $0.1 LAI$ and $w_{\text{vegt}} = [W_{\text{leaf}}/(0.1 LAI)]^{2/3}$. Any excess water from the leaf reservoir is then included in Rnd_- so that it can enter the soil reservoir.

An advantage with in-canyon vegetation parametrizations is that it is straightforward to include the interactions between wall, road and vegetation energy budgets. For example, building shadowing effects modify the shortwave radiation absorbed by the vegetation canopy, as well as the vegetation modifying the albedo of the canyon floor (see Appendix). Canyon surface temperatures are also decreased with in-canyon vegetation, since the vegetation can absorb longwave and sensible heat from walls and roads and re-partition some of this energy into latent heat. An example of this is shown in Fig. 2, where we show the road and wall surface temperatures for cases were vegetation is included within the canyon, and when vegetation fluxes are evaluated independently outside the canyon (i.e., using a tiling approach with the host atmospheric model's vegetation canopy scheme). The road and wall surface temperatures are lower by 0.7–2°C on average, respectively, for the experiment with in-canyon vegetation and are consistent with the results obtained by Lee and Park (2008). The cooling of urban canyon surfaces has occurred despite the air temperature at the first atmospheric model level being slightly greater for the in-canyon vegetation experiment by 0.1°C on average (not shown).

2.4 Modification of Canyon Fluxes with Two Canyon Walls

A number of parametrizations of in-canyon turbulent heat fluxes have been proposed for various UCMs (e.g., Masson (2000), Kusaka et al. (2001)), typically based on in-situ

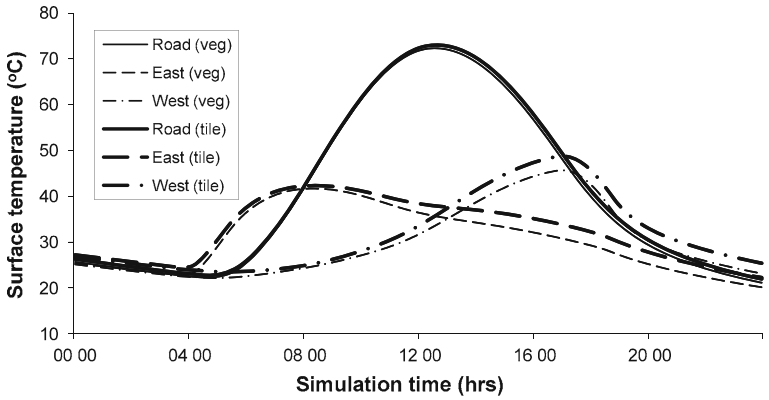

Fig. 2 Plot of the surface temperature for roads (*continuous lines*), east facing walls (*dashed lines*) and west facing walls (*dot-dashed lines*) when vegetation is included in the canyon (*thin lines* denoted by 'veg'), compared to a tiling approach where vegetation is simulated independently outside the canyon (*bold lines* denoted by 'tile')

measurements or wind-tunnel experiments. An alternative process based parametrization of in-canyon turbulent heat fluxes was proposed by Harman et al. (2004b), which is formulated around how the air is recirculated and vented within the canyon. The scheme was found to agree well with wind-tunnel observations, including predicted changes in fluxes when the canyon aspect ratio, h/w, is modified. Estimating turbulent heat fluxes for additional canyon surfaces (e.g., in-canyon vegetation), is also relatively straightforward with this scheme. As the parametrization from Harman et al. (2004b) results in different fluxes for walls on either side of the canyon, then to include it in our UCM also requires separate canyon wall energy budgets. Unlike previous UCMs, we construct the two canyon wall energy budgets by integrating the canyon over 180° of possible orientations so that the canyon walls separate into walls with an east-facing component and walls with a west-facing component. As a result, we can successfully separate the two canyon wall energy budgets while avoiding the need to assign a favoured orientation of the urban canyon.

Integrating the canyon over 180° of possible orientations has implications for both the partitioning of radiation and the calculation of fluxes within the canyon. This is because these quantities depend on the effective width of the canyon, which in turn depends on the relative orientation of the canyon with respect to the solar azimuthal angle, θ_a, and with respect to the wind direction, θ_w. The two extreme cases then occur when the solar azimuthal angle or wind direction is parallel with the orientation of the canyon and when these angles are perpendicular to the orientation of the canyon. To illustrate these issues, in this section we focus on how the aerodynamic resistances are calculated using the parametrization from Harman et al. (2004b), when the canyon is integrated over 180° of possible canyon orientations. Modifications to the partitioning of shortwave and longwave radiation arising from the two canyon wall energy budgets are described in the Appendix.

In-canyon sensible heat fluxes are calculated using the expression

$$H_* = \rho_a C_a \left(T_* - T_{can}\right) / \Omega_*, \tag{22}$$

where $* =$ road, east, west, vegt and Ω_* is the aerodynamic resistance for the in-canyon surfaces. In contrast, the only sources of latent heat flux in the canyon are from in-canyon vegetation (see Sect. 2.3), and water on the surface of the road. The latent heat flux due to water on the road surface is calculated using the expression

$$LE_{\text{road}} = w_{\text{road}} \rho_{\text{a}} L_{\text{v}} \left(\text{qsat}_{\text{road}} - q_{\text{can}}\right) / \Omega_{\text{road}}, \tag{23}$$

where $\text{qsat}_{\text{road}}$ is the saturated mixing ratio for the road and w_{road} denotes the fraction of the road covered by water (see Appendix). We estimate the aerodynamic resistance, Ω_*, in terms of the roughness length, $z_{0,*}$, and the wind speed along a canyon surface, v_*, using the expression based on Harman et al. (2004b)

$$\frac{1}{\Omega_*} = \frac{\kappa^2 v_*}{\ln(0.1h/z_{0*})(2.3 + \ln(0.1h/z_{0*}))}, \tag{24}$$

where $^* =$ road, wall, vegt. Note that in our UCM, the in-canyon vegetation has a larger roughness length ($z_{0,\text{vegt}} = 0.1$ m) than the road or wall surfaces ($z_{0,\text{road}} = z_{0,\text{wall}} = 0.01$ m), with a corresponding change in the aerodynamic resistance.

To calculate the in-canyon wind speeds, v_*, we start by estimating the wind speed at the top of the urban canyon, v_{top}, using standard MOST with the roughness length for the urban area, $z_{0,\text{urbn}}$. Following Harman et al. (2004b), the venting regions are separated by a jet whose position and speed is determined by the wind speed at the canyon top and the canyon geometry (i.e., height, h, and width, w). The length of the jet, L_{se}, and the speed of the jet when it reaches a canyon surface, v_0, is then calculated according to

$$v_0 = v_{\text{top}} \exp(-\alpha_1 L_{\text{se}}/h), \tag{25}$$

$$L_{\text{se}} = \begin{cases} \sqrt{13/4}h & w' \geq 3h \\ \sqrt{13/4}\Delta h & w' < 3h, \end{cases} \tag{26}$$

where $\Delta h = \max(2w'/3 - h, 0)$ and $\alpha_1 = 0.9$ as specified by Harman et al. (2004b). Note that we have introduced $w' = w/\sin(\theta - \theta_w)$, which indicates the effective canyon width for a canyon orientation of θ and a wind direction of θ_w. This allows us to integrate the aerodynamic resistances over all possible canyon orientations later in this section. The length and speed of the jet depends on whether the jet impinges on the road ($w' \geq 3h$) or the canyon wall ($w' < 3h$). Harman et al. (2004b) estimate the wind speed on a given canyon facet as

$$v_{\text{S}} = \frac{v_0}{b} \int_{\text{a}}^{a+b} \exp\left(-\alpha_2 x/h\right) \mathrm{d}x, \tag{27}$$

where a is the distance travelled to the start of the canyon facet, b is the distance travelled along the facet and $\alpha_2 = 0.15 \max(1, 1.5h/w')$. Using Eq. 27 we can estimate the representative wind speeds for the canyon floor, v_{F}, the recirculation wall, v_{R}, and the venting wall, v_{V}. In the case where the jet impinges on the canyon floor ($w' \geq 3h$)

$$v_{\text{F}}^{\text{A}} = \frac{u_0 h}{\alpha_2 w'}\{2 - \exp(-3\alpha_2) - \exp[-\alpha_2(w'/h - 3)]\}, \tag{28}$$

$$v_{\text{V}}^{\text{A}} = \frac{u_0}{\alpha_2} \exp[-\alpha_2(w'/h - 3)][1 - \exp(-\alpha_2)], \tag{29}$$

$$v_{\text{R}}^{\text{A}} = \frac{u_0}{\alpha_2} \exp(-3\alpha_2)[1 - \exp(-\alpha_2)]. \tag{30}$$

For the second case where the jet impinges on the canyon wall ($w' < 3h$), v_{F}, v_{R} and v_{V} become

$$v_{\text{F}}^{\text{B}} = \frac{u_0 h}{\alpha_2 w'} \exp[-\alpha_2(1 - \Delta h'/h)][1 - \exp(-\alpha_2 w'/h)], \tag{31}$$

$$v_{\text{V}}^{\text{B}} = \frac{u_0}{\alpha_2}\{2 - \exp[-\alpha_2(1 - \Delta h'/h)] - \exp(-\alpha_2 \Delta h/h)\}, \tag{32}$$

$$v_{\mathrm{R}}^{\mathrm{B}} = \frac{u_0}{\alpha_2} \exp[-\alpha_2(1 - \Delta h'/h + w/h)][1 - \exp(-\alpha_2)]. \tag{33}$$

The superscripts A and B then indicate the jet impinging on the canyon floor and jet impinging on the wall, respectively. Note that the wind speed for the venting wall and the canyon floor is based on a weighted average of the venting region and recirculation region wind speeds. This effectively averages the venting and recirculation aerodynamic resistances since the sensible heat flux is proportional to the wind speed along the in-canyon surfaces. The minimum wind speed is also limited due to the mixing of high momentum air down into the venting region of the canyon, as explained in Harman et al. (2004b).

To calculate the average wind speeds on the canyon surfaces, we need to integrate the different canyon orientations over 180°. Note that we expect that the jet will impinge on the canyon wall for some canyon orientations, if the effective canyon width w' is narrow enough. However, there will always be orientations where the jet impinges on the canyon floor (e.g., when $\theta = \theta_w$, so that $w' \to \infty$). We can then introduce an angle, Θ_1, which determines the critical angle of the canyon orientation when the jet is first incident on the canyon floor. Note that Θ_1 is analogous to Θ_0 introduced by Masson (2000), where Θ_0 is the critical angle when shortwave radiation is incident on the canyon floor. Θ_1 is calculated as

$$\cos(\Theta_1) = \min(w/3h, 1). \tag{34}$$

We then partition the calculation of in-canyon winds into east- and west-facing walls as well as when the jet impinges on the canyon wall or on the canyon floor. The resultant wind speeds are then ($0 \leq \theta_w < \pi$)

$$\begin{aligned} 2v_{\mathrm{surf}} = & \int_{0}^{\max(0,\theta_w-\pi+\Theta_1)} v_{\mathrm{F}}^{\mathrm{A}} \sin(\theta - \theta_w)\mathrm{d}\theta + \int_{\max(0,\theta_w-\pi+\Theta_1)}^{\max(0,\theta_w-\Theta_1)} v_{\mathrm{F}}^{\mathrm{B}} \sin(\theta - \theta_w)\mathrm{d}\theta \\ & + \int_{\max(0,\theta_w-\Theta_1)}^{\min(\pi,\theta_w+\Theta_1)} v_{\mathrm{F}}^{\mathrm{A}} \sin(\theta - \theta_w)\mathrm{d}\theta + \int_{\min(\pi,\theta_w+\Theta_1)}^{\min(\pi,\theta_w+\pi-\Theta_1)} v_{\mathrm{F}}^{\mathrm{B}} \sin(\theta - \theta_w)\mathrm{d}\theta \\ & + \int_{\min(\pi,\theta_w+\pi-\Theta_1)}^{\pi} v_{\mathrm{F}}^{\mathrm{A}} \sin(\theta - \theta_w)\mathrm{d}\theta, \end{aligned} \tag{35}$$

$$\begin{aligned} 2v_{\mathrm{east}} = & \int_{0}^{\max(0,\theta_w-\pi+\Theta_1)} v_{\mathrm{V}}^{\mathrm{A}} \sin(\theta - \theta_w)\mathrm{d}\theta + \int_{\max(0,\theta_w-\pi+\Theta_1)}^{\max(0,\theta_w-\Theta_1)} v_{\mathrm{V}}^{\mathrm{B}} \sin(\theta - \theta_w)\mathrm{d}\theta \\ & + \int_{\max(0,\theta_w-\Theta_1)}^{\theta_w} v_{\mathrm{V}}^{\mathrm{A}} \sin(\theta - \theta_w)\mathrm{d}\theta + \int_{\theta_w}^{\min(\pi,\theta_w+\Theta_1)} v_{\mathrm{R}}^{\mathrm{A}} \sin(\theta - \theta_w)\mathrm{d}\theta \\ & + \int_{\min(\pi,\theta_w+\Theta_1)}^{\min(\pi,\theta_w+\pi-\Theta_1)} v_{\mathrm{R}}^{\mathrm{B}} \sin(\theta - \theta_w)\mathrm{d}\theta + \int_{\min(\pi,\theta_w+\pi-\Theta_1)}^{\pi} v_{\mathrm{R}}^{\mathrm{A}} \sin(\theta - \theta_w)\mathrm{d}\theta, \end{aligned} \tag{36}$$

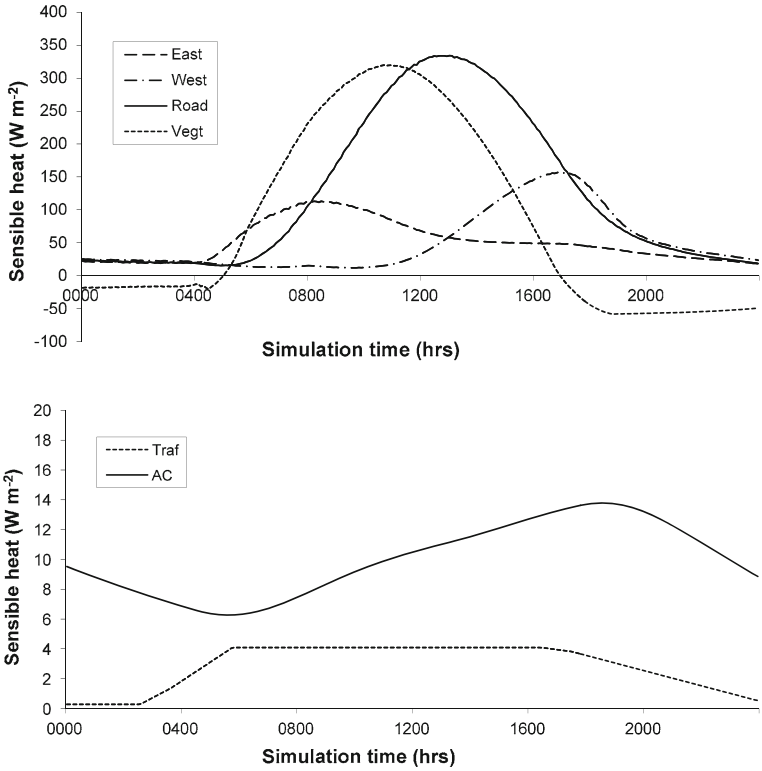

Fig. 3 Sensible heat flux from different sources within the canyon for a typical day in January for Melbourne, Australia. Due to the different magnitudes involved, the plot is divided into two scales with the road (*solid line*), east wall (*dash line*), west wall (*dash dot line*) and vegetation (*dot line*) on the *top plot*. The flux due to air-conditioning (*solid line*) and traffic (*dot line*) is shown on the *bottom plot*

$$
\begin{aligned}
2v_{\text{west}} = &\int_{0}^{\max(0,\theta_w-\pi+\Theta_1)} v_{\text{R}}^{\text{A}} \sin(\theta-\theta_w)\mathrm{d}\theta + \int_{\max(0,\theta_w-\pi+\Theta_1)}^{\max(0,\theta_w-\Theta_1)} v_{\text{R}}^{\text{B}} \sin(\theta-\theta_w)\mathrm{d}\theta \\
&+ \int_{\max(0,\theta_w-\Theta_1)}^{\theta_w} v_{\text{R}}^{\text{A}} \sin(\theta-\theta_w)\mathrm{d}\theta + \int_{\theta_w}^{\min(\pi,\theta_w+\Theta_1)} v_{\text{V}}^{\text{A}} \sin(\theta-\theta_w)\mathrm{d}\theta \\
&+ \int_{\min(\pi,\theta_w+\Theta_1)}^{\min(\pi,\theta_w+\pi-\Theta_1)} v_{\text{V}}^{\text{B}} \sin(\theta-\theta_w)\mathrm{d}\theta + \int_{\min(\pi,\theta_w+\pi-\Theta_1)}^{\pi} v_{\text{V}}^{\text{A}} \sin(\theta-\theta_w)\mathrm{d}\theta, \quad (37)
\end{aligned}
$$

with the definitions of v_{east} and v_{west} reversed when $-\pi \leq \theta_w < 0$. In our model, Eqs. 35–37 are solved numerically, which allows us to be flexible in the design of the in-canyon aerodynamic resistances (i.e., for future extensions to the model). Finally, we note that the east and west facing walls sensible heat fluxes were coupled in Eq. 4. This situation arises since both cases occur with the jet impinging on the canyon wall ($w' < 3h$) and with the jet impinging on the canyon floor ($w' \geq 3h$), during the integration of the different canyon orientations in Eqs. 35–37.

Figure 3 shows the sensible heat flux from different surfaces within the canyon for a typical day in January (i.e., H_{east}, H_{west}, H_{road}, H_{vegt}, H_{traf} and H_{AC}). Note that calculating H_{can} requires the sensible heat fluxes in Fig. 3 to be weighted by δ_{vegt} and h/w terms as described in Eq. 4. The greatest contributions to the in-canyon sensible heat flux budget arise from the road, walls and vegetation terms. In particular, we note differences in the diurnal behaviour of the walls, road and vegetation. East-facing walls heat first with the rising sun, whereas the west-facing walls cool last with the setting sun. Note that, if the sensible heat fluxes from the two walls are combined, then we obtain two local maxima, corresponding to the maximum for the east-facing wall and the maximum from the west-facing wall. For this reason we have chosen to separate the canyon wall energy budget into east-facing and west-facing walls. We also observe that since the in-canyon vegetation cannot store heat (see Eq. 3), it warms more quickly than the road, resulting in a relative lag between the peak in H_{vegt} compared to H_{road}. The air-conditioning flux, H_{AC} is comparable in magnitude to the traffic sensible heat flux, with the peak value being relatively small compared to the maximum sensible heat flux from roads, vegetation or walls.

3 TAPM Technical Description

To provide the atmospheric forcings for the UCM and for nesting in NCEP reanalyses, we have used TAPM v4.03 (Hurley et al. 2005; Hurley and Luhar 2009). The TAPM model was chosen for this task as it supports a prognostic meteorological model that is used to downscale reanalyses to local urban length scales, as well as supporting a prognostic air quality model. TAPM includes both hydrostatic and (optionally) non-hydrostatic contributions to the pressure as well as prognostic equations for the conservation and continuity of momentum, heat and moisture for simulating winds, potential virtual temperature and specific humidity. A gradient diffusion approach with counter-gradient correction is used for the turbulence closure of temperature and moisture, where eddy diffusivity is calculated from the prognostic turbulence kinetic energy and prognostic eddy dissipation rate, as well as a mass-flux approach used to calculate the counter-gradient term (Hurley 2007). TAPM includes physical parametrizations for cloud microphysics (water vapour, cloud water, cloud ice, rain and snow), radiation and a soil-canopy surface scheme with vegetation overlaying soil for radiation and surface fluxes. Prognostic equations to simulate soil heat diffusion and Richards' equation for soil moisture are included to model soil to a depth of 2 m using 15 layers. Orography and landuse are derived from the United States Geological Survey 1-km resolution datasets. Note that radiative feedbacks due to urban pollution are currently not accounted for and TAPM's dispersion modelling capacity is not employed in this study.

TAPM employs a multiple one-way nesting procedure to dynamically downscale meteorological reanalyses, typically in steps of 30 km, 10 km and 3 km. In TAPM, Davies (1976) lateral boundary conditions are applied to the horizontal wind components, virtual potential temperature and specific humidity. Global nudging is also applied to the horizontal wind components and virtual potential temperature at all grid points with a 24 hour e-folding time. TAPM was configured with 25 $\times$ 25 horizontal grid points at 30 km, 10 km and 3 km grid spacing. TAPM also includes 25 vertical levels at terrain following levels of 10 m, 25 m, 50 m, 100 m, 150 m, 200 m, 250 m, 300 m, 400 m, 500 m, 600 m, 750 m, 1 km, 1.25 km, 1.5 km, 1.75 km, 2 km, 2.5 km, 3 km, 3.5 km, 4 km, 5 km, 6 km, 7 km and 8 km. This configuration of TAPM produces one year of simulated data in approximately six hours, while still resolving the planetary boundary layer above the urban environment in acceptable detail.

4 Evaluation of the Simulated Urban Climate

In this section we evaluate the performance of the UCM described in Sect. 2 for predicting the urban climatology when coupled to the TAPM atmospheric model described in Sect. 3. We also compare the UCM results to the standard TAPM urban scheme, which is based on a slab urban model (Oke 1988). To distinguish between the different urban parametrizations, we use the labels 'canyon' and 'slab' for the UCM described herein and the original TAPM slab urban model, respectively. To evaluate the performance of the urban parametrizations, we use TAPM to downscale NCEP analyses for the year 2003 to a 3-km resolution over Melbourne, Australia. In this way, NCEP analyses are employed as an idealized general circulation model with minimal errors in the boundary forcing. The domain and orography used for the 3-km resolution TAPM simulation is shown in Fig. 4, along with the locations of the three Environmental Protection Agency (EPA) monitoring stations. These stations where chosen to represent a mixture of inner city (Alphington), coastal (Brighton) and urban fringe (Melton) locations, where Alphington, Brighton and Melton are abbreviated as ALP, BRI and MEL. The simulation grid is centred on 144°58′ longitude and −38°49′ latitude. We have deliberately used the same generic urban parameters for all urban grid points, as defined in the Appendix, because we wish to evaluate the model performance when simulating a

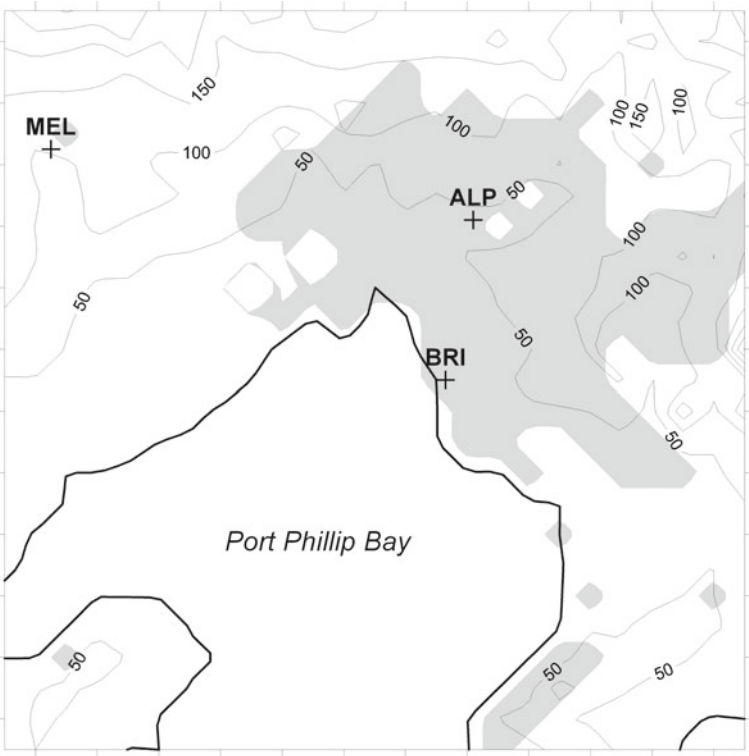

Fig. 4 Location of three EPA monitoring station sites situated around Melbourne (144°58′E and 38°49′S). *Contours* indicate the height of the orography, with a *bold contour* indicating the coastline surrounding Port Phillip Bay. *Grey shading* denotes the areas of urban land use. The figure also shows the $75 \times 75\,\text{km}^2$ domain used for the 3-km resolution TAPM simulation

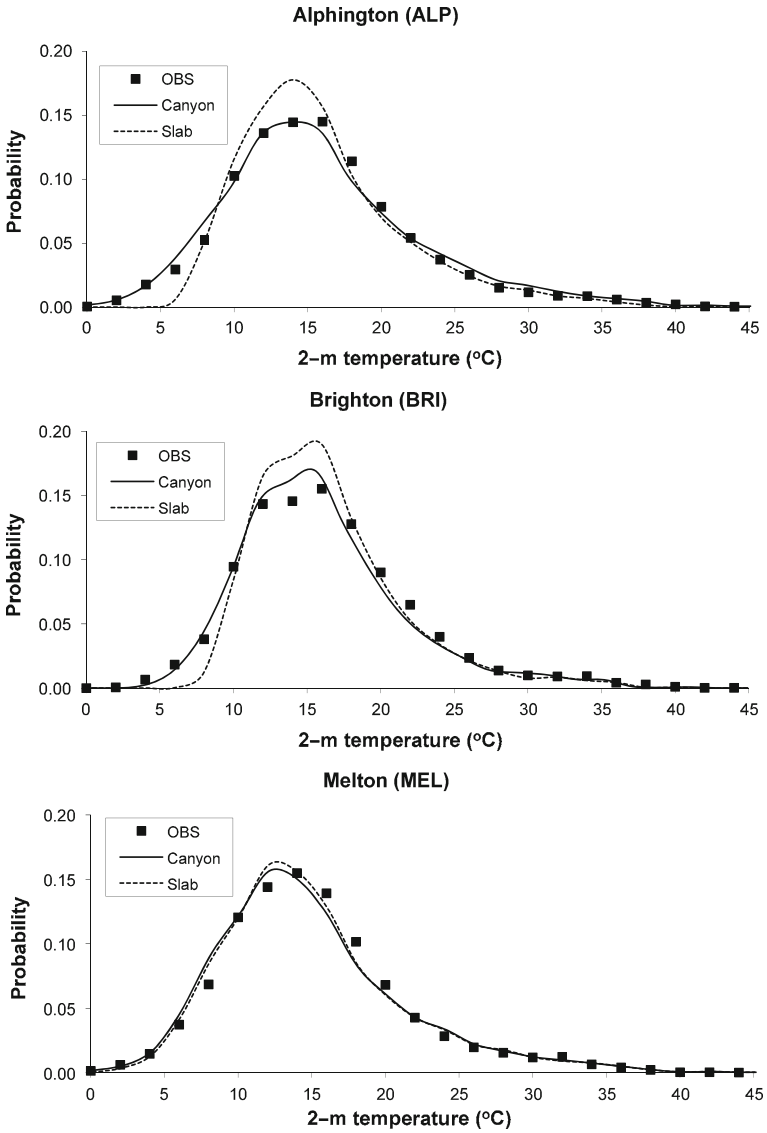

Fig. 5 Simulated and observed screen temperature climatology for the three EPA monitoring station sites located around Melbourne. Canyon and Slab indicates the UCM described in Sect. 2 and TAPM's default slab urban model, respectively. The MEL site is modelled using mid-dense pasture for both the Canyon and Slab experiments

generic Australian city, and therefore the simulation is still applicable for modelling a future climate for which the composition of the urban environment may have changed. The ALP and BRI sites are located in generic urban grid points, while the urban fringe MEL site is located in a grid box that is assigned a vegetative land-use category (i.e., mid-dense pasture).

The probability distribution functions (PDFs) obtained for the observed and simulated screen temperatures are shown in Fig. 5 for the three EPA monitoring stations, where we

Table 1 Simulated and observed screen temperature and 10-m wind speeds for the Alphington EPA monitoring station

Variable	Model	DJF	MAM	JJA	SON
T_{max} (°C)	**Obs**	**27.1**	**21.2**	**14.7**	**19.5**
	Canyon	27.1	19.9	14.5	18.9
	Slab	26.4	19.8	14.6	18.8
T_{min} (°C)	**Obs**	**14.4**	**10.5**	**6.4**	**8.0**
	Canyon	14.1	9.7	5.7	8.1
	Slab	14.0	11.9	7.8	9.2
U wind ($m\,s^{-1}$)	**Obs**	**0.5**	**0.1**	**0.5**	**0.7**
	Canyon	0.5	0.2	0.7	1.0
	Slab	0.4	0.2	0.7	0.9
V wind ($m\,s^{-1}$)	**Obs**	**1.0**	**0.4**	**−1.7**	**0.2**
	Canyon	0.9	0.1	−1.9	−0.1
	Slab	0.7	0.1	−1.6	−0.1

Seasons are denoted as DJF, MAM, JJA and SON for December–January–February, March–April–May, June–July–August, September–October–November, respectively. Obs, Canyon and Slab indicates observations, the UCM described in Sect. 2 and TAPM's default slab urban model, respectively. Observations are indicated in bold type

also show the observed and simulated seasonal climatology in Tables 1, 2, 3 for ALP, BRI and MEL, respectively. The observed climatology is estimated from hourly data measured during 2003, hence the simulated results are also based on hourly data for the same time period. Figure 5 suggests a reasonable representation of the current screen temperature PDF by the canyon UCM for all three locations considered, where the modelled average screen temperature is within 0.3 of the observed value at the urban sites ALP and BRI, and within 0.4°C at the rural MEL site. The variability in the screen temperature is slightly overestimated by the canyon model, with the simulated standard deviation being 0.2°C larger than the observed value. There is also a tendency for the canyon UCM to underestimate the minimum temperature (see Tables 1, 2, 3). These results can be compared to the slab model that significantly overestimates the minimum temperature, thereby underestimating the frequency of low temperatures in Fig. 5. As a consequence, the slab model underestimates the temperature standard deviation by 0.8°C for the urban ALP and BRI sites. Hence, the canyon UCM has significantly improved the simulated variability in screen temperature by better representing the minimum temperatures than the slab UCM. Since the MEL site is specified as a vegetative land-use category (i.e., rural), then both urban parametrizations give similar results at this site.

Figures 6 and 7 compare the observed 10-m wind speed and wind direction climatology with the simulated climatology from the canyon UCM and TAPM's slab urban model. The predicted wind speed for different seasons are also compared to observations at the EPA monitoring stations in Tables 1, 2, 3. The average wind speed and its standard deviation seem to be reasonably well simulated by the canyon UCM, with the predicted average wind speed and standard deviation being within 0.5 and $0.1\,m\,s^{-1}$ of the observed values, respectively. This can be compared to the results of the slab model for which the predicted average wind speed and standard deviation is within 0.3 and $0.3\,m\,s^{-1}$, respectively. Figure 6 indicates that the simulated low wind speeds ($<2\,m\,s^{-1}$) are somewhat underrepresented in the simulated PDFs, although this problem also occurs for non-urban locations (e.g., MEL). The under representation of low wind speeds used to be a common problem for TAPM v3, but has been

Table 2 Simulated and observed screen temperature and 10-m wind speeds for the Brighton EPA monitoring station

Variable	Model	DJF	MAM	JJA	SON
T_{max} (°C)	**Obs**	**26.3**	**20.8**	**14.8**	**19.4**
	Canyon	25.4	19.4	14.5	18.3
	Slab	25.1	19.5	14.7	18.4
T_{min} (°C)	**Obs**	**15.4**	**11.6**	**7.8**	**9.6**
	Canyon	15.1	11.6	7.8	9.9
	Slab	15.1	13.2	9.2	10.6
U wind ($m\,s^{-1}$)	**Obs**	**0.4**	**0.1**	**0.5**	**0.9**
	Canyon	0.5	0.2	1.2	1.4
	Slab	0.4	0.2	1.2	1.3
U wind ($m\,s^{-1}$)	**Obs**	**1.3**	**0.5**	**−1.9**	**0.1**
	Canyon	1.5	0.5	−2.2	0.2
	Slab	1.3	0.5	−2.0	0.2

Labels are the same as used for Table 1

Table 3 Simulated and observed screen temperature and 10-m wind speeds for the Melton EPA monitoring station

Variable	Model	DJF	MAM	JJA	SON
T_{max} (°C)	**Obs**	**25.6**	**19.9**	**13.7**	**17.7**
	Canyon	26.4	18.2	13.7	18.1
	Slab	26.3	18.2	13.7	18.2
T_{min} (°C)	**Obs**	**13.7**	**10.0**	**6.2**	**7.5**
	Canyon	12.0	9.2	5.6	7.1
	Slab	12.7	10.3	5.9	7.4
U wind ($m\,s^{-1}$)	**Obs**	**0.4**	**0.7**	**1.2**	**1.4**
	Canyon	0.5	0.8	1.8	1.8
	Slab	0.5	0.8	1.8	1.7
V wind ($m\,s^{-1}$)	**Obs**	**1.1**	**0.3**	**−2.2**	**−0.1**
	Canyon	1.0	0.1	−2.6	−0.2
	Slab	0.9	0.2	−2.5	−0.2

Labels are the same as used for Table 1

improved in TAPM v4.03 (see (Hurley et al. 2005; Hurley and Luhar 2009) for details). The predominance of northerly and southerly wind directions appears to be well reproduced by both urban parametrizations (Fig. 7), although the representation of easterly winds is under-represented at the ALP site to some extent. However, the increased frequency of westerly winds at the MEL site is successfully reproduced by the simulation.

To evaluate the energy partitioning of the canyon UCM from Sect. 2, we compare the simulated urban fluxes to flux-tower measurements for the Melbourne area made by Coutts et al. (2007) during 2004. These flux tower experiments were made from 1000 to 1600 local time, with the flux-tower sites categorised as HIGH, MEDIUM, LOW and RURAL. The generic urban parameters used for the ALP and BRI sites are based on the MEDIUM urban category from Coutts et al. (2007), whereas the MEL site more closely resembles the RURAL category. Note that the simulated and observed results correspond to different locations and time periods, with both the simulation and the observations taking place during a period of extended drought. Nevertheless, there is some agreement between the simulated and measured climatology of net radiation, Q^*, sensible heat flux, Q_H, and latent heat flux, Q_E, shown in Fig. 8. The storage flux ΔQ_S can be estimated according to

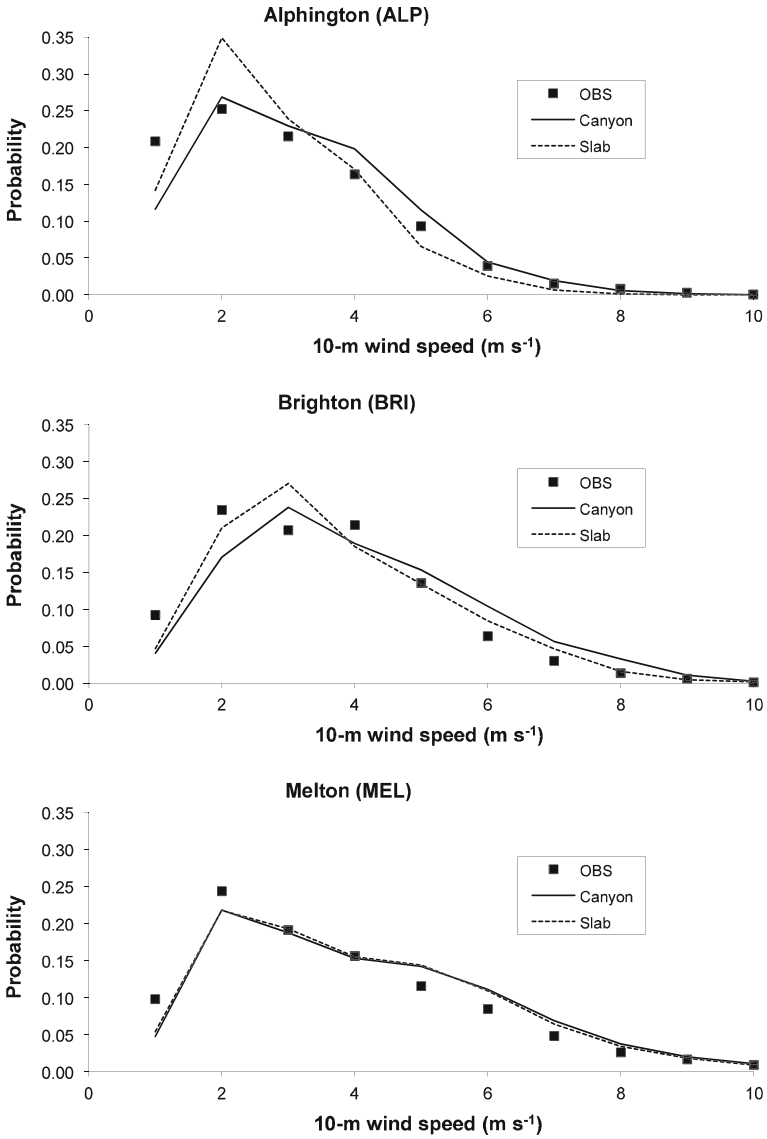

Fig. 6 Simulated and observed 10-m wind speed climatology for the three EPA monitoring station sites located around Melbourne. Canyon and Slab indicates the UCM described in Sect. 2 and TAPM's default slab urban model, respectively. The MEL site is modelled using mid-dense pasture for both the Canyon and Slab experiments

$$Q^* = Q_H + Q_E + \Delta Q_S, \tag{38}$$

where we assume that the additional anthropogenic heat flux (i.e., other than traffic, heating and cooling) and advective heat flux are negligible. Hence, we do not plot the storage flux in Fig. 8 as it can be inferred from the result of the other fluxes. The results in Fig. 8 show that the simulated net radiation is typically 20–30 $\mathrm{W\,m^{-2}}$ greater than observed for the MEDIUM site, with a similar difference also occurring at the rural MEL site. Otherwise the timing

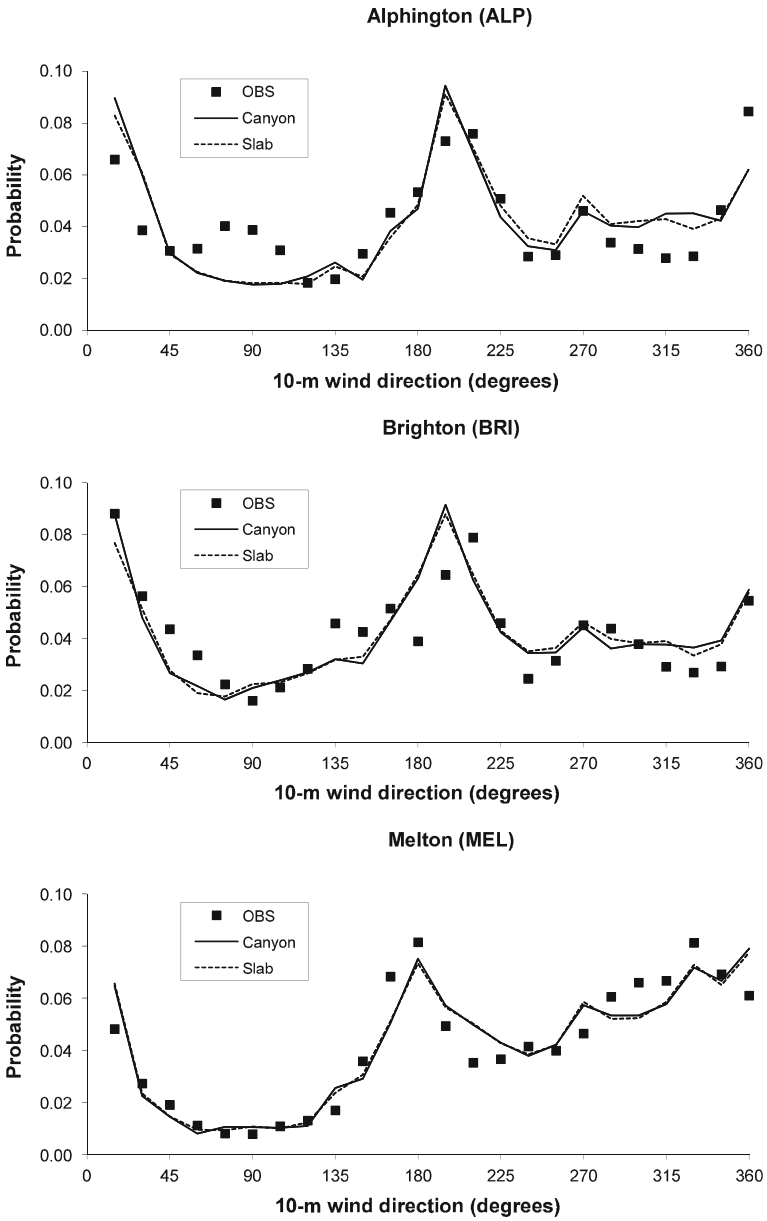

Fig. 7 Simulated and observed 10-m wind direction climatology for the three EPA monitoring station sites located around Melbourne. Canyon and Slab indicates the UCM described in Sect. 2 and TAPM's default slab urban model, respectively. The MEL site is modelled using mid-dense pasture for both the Canyon and Slab experiments

of peaks and troughs is similar between the simulations and observations. The simulated sensible heat flux is overestimated by the model during summer, although similar errors are observed for the MEL rural site. The latent heat flux is reasonably well represented by the

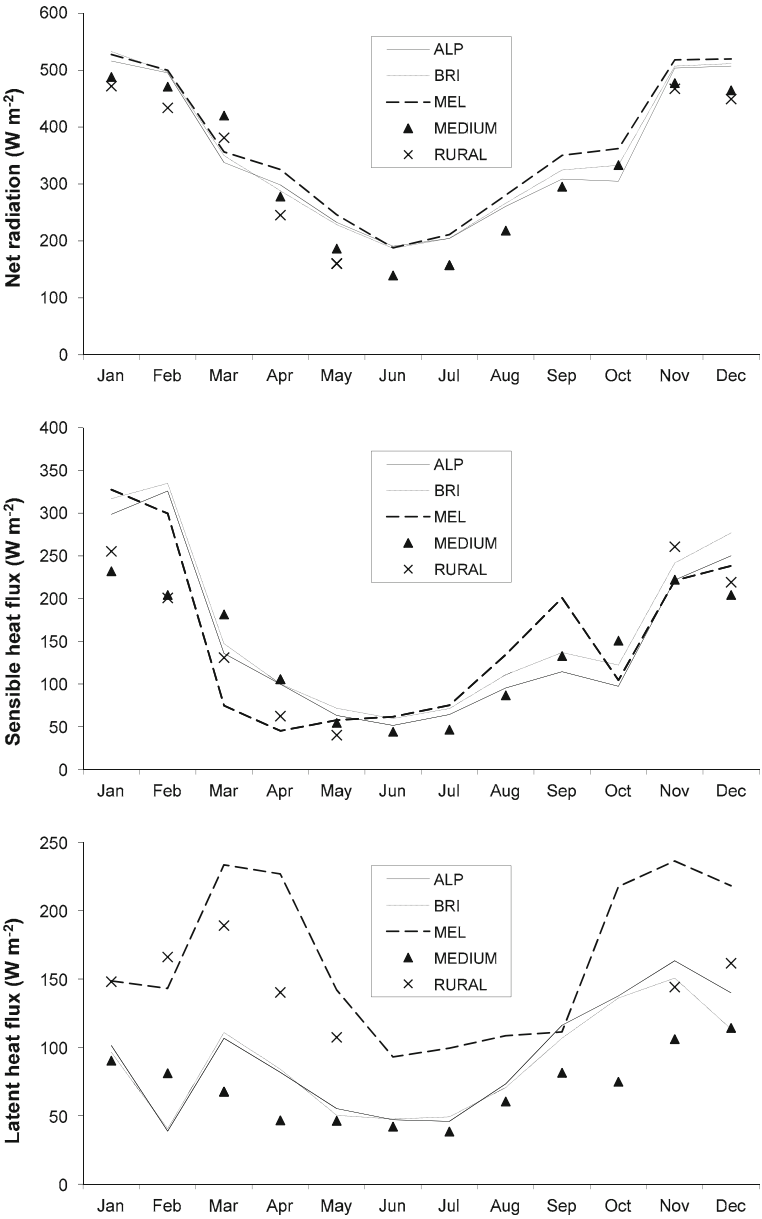

Fig. 8 Simulated intra-annual variation of surface energy fluxes for the canyon based UCM described herein. The fluxes are plotted for locations corresponding to the location of EPA monitoring stations and are averaged between 1000 to 1600 local time

UCM, although the model appears to underestimate the latent heat flux in February (possibly due to neglecting irrigation of suburban gardens) and overestimates the latent heat flux in spring. The model does correctly predict the reduced latent heat flux for the urban (i.e., ALP and BRI) sites compared to the non-urban (i.e., MEL) site, as shown in the observations.

Furthermore, the model correctly predicts a greater storage flux for urban sites compared to non-urban sites (not shown), but underestimates the annual amplitude.

5 Conclusions

We have developed an urban canopy model (UCM) for studying the urban climate of Australian cities. Our scheme follows the TEB approach of Masson (2000), but with modifications to provide a computationally efficient representation of suburban areas in regional climate simulations. The UCM is prevented from acting as an energy sink during the Australian summer by introducing a simple parametrization of an idealized air-conditioner. Our UCM supports in-canyon coupling between vegetation and urban surfaces, but employs a reduced set of prognostic variables after assuming 100% vegetation cover over bare soil within the canyon. Thirdly, we have solved for two canyon-wall energy budgets by integrating the canyon over 180° of possible orientations. This approach allows us to use the parametrization of in-canyon turbulent heat fluxes proposed by Harman et al. (2004b) to couple vegetation with canyon walls and road energy budgets, but without the need to specify a fixed canyon orientation within the grid box. The resultant UCM is then designed to be computationally efficient and energy conserving when applied to regional climate simulations, without degrading the accuracy of the simulation.

Using the UCM, we simulate the urban climate of Melbourne at 3-km resolution for one year after nesting the UCM in the TAPM atmospheric model. The results suggest a good representation of the urban screen temperature and 10-m wind speed climatology. In particular, the average temperature is within 0.3°C for all monitoring sites considered in this paper. The average simulated wind speed is also within $0.5\,\mathrm{m\,s^{-1}}$ for all sites that were examined. The predominately northerly and southerly wind directions are reproduced by the model, although the frequency of easterly winds is underestimated for the Alphington site. The UCM was found to predict the frequency of low air temperatures much better than TAPM's standard slab urban scheme, which systematically overestimates the daily minimum air temperatures. Plots of the energy partitioning of the urban environment suggest that the UCM does provide a plausible representation of the urban energy budget when compared to flux-tower measurements by Coutts et al. (2007). The intra-annual variation in the fluxes also suggests that the seasonal behaviour of the model is reasonable. The net radiation is typically larger than that observed for a MEDIUM urban site and the sensible heat flux is overestimated in summer to an extent, although similar errors in fluxes are observed for the rural site. An improved representation of inner city types could potentially be achieved by using different parameters to represent different urban landuse categories. Nevertheless, we have used generic urban parameters in this study so as to be appropriate for studying future urban climates for which the detailed urban composition is unknown.

Acknowledgments The authors would like to thank Ashok Luhar, Jack Katzfey, John McGregor, Eva Kowalczyk and Ying-Ping Wang for their helpful comments concerning this manuscript. The authors also thank the two anonymous reviewers for their constructive comments. Thanks also to the EPA Victoria for supplying the monitoring data used in this work.

Appendix

We describe the partitioning of shortwave radiation, longwave radiation, conduction and water on urban surfaces.

A1. Shortwave radiation

The partitioning of shortwave radiation follows an approach similar to Kanda et al. (2005), where we numerically solve for the reflections up to third order. It is possible to solve for infinite reflections (e.g., Harman et al. 2004a), however such methods can be computationally expensive to update every time step if the albedo is changing within the canyon (e.g., due to snow). Nevertheless, the results of Harman et al. (2004a) do suggest that including up to third-order reflections is adequate for the canyon geometry considered. The shortwave radiation incident on an urban canyon surface can be expressed as

$$S_* = (1 - \alpha_*) \sum_{i=0}^{N_r} s_{*,i}, \tag{39}$$

where α_* is the albedo for * = road, wall, vegt surfaces. For surfaces within the urban canyon, we need to calculate the shortwave reflections as indexed by i for a maximum of N_r reflections (i.e., $N_r = 3$ in our model). The incident shortwave radiation on the urban surfaces is calculated by (i.e., $i = 0$)

$$s_{\mathrm{surf},0} = (2/\pi)\{\Theta_0 - (h/w)\tan(\theta_z)[1 - \cos(\Theta_0)]\} S^{\mathrm{D}}_{\mathrm{in}} + \psi_{\mathrm{surf}} S^{\mathrm{d}}_{\mathrm{in}}, \tag{40}$$

$$s_{\mathrm{east},0} = (1/\pi)\{(\pi - 2\Theta_0 - X)(w/h) + \tan(\theta_z)[2 - 2\cos(\Theta_0) - Y]\} S^{\mathrm{D}}_{\mathrm{in}} + \psi_{\mathrm{wall}} S^{\mathrm{d}}_{\mathrm{in}}, \tag{41}$$

$$s_{\mathrm{west},0} = (1/\pi)\left[X(w/h) + \tan(\theta_z)Y\right] S^{\mathrm{D}}_{\mathrm{in}} + \psi_{\mathrm{wall}} S^{\mathrm{d}}_{\mathrm{in}}, \tag{42}$$

where $S^{\mathrm{D}}_{\mathrm{in}}$ and $S^{\mathrm{d}}_{\mathrm{in}}$ are the direct and diffuse components of downwelling shortwave radiation from the host atmospheric model, respectively, and θ_z is the solar zenith angle. In the case of the roof, we simply set $S_{\mathrm{roof}} = (1 - \alpha_{\mathrm{roof}})S_{\mathrm{in}}$, as there are no additional reflections with other canyon surfaces that need to be accounted for. As discussed by Masson (2000), Θ_0 determines the critical angle of the canyon orientation when shortwave radiation is incident on the canyon floor and can be written as $\sin(\Theta_0) = \max[(h/w)\tan(\theta_z), 1]^{-1}$.

Equations 41–42 differ from those described in Masson (2000), since we have introduced X and Y to account for the change in the partitioning of shortwave radiation arising from integrating the canyon over 180° of possible orientations instead of 360°. X indicates the relative amount of east-facing walls that are facing the sun and that the road is in shadow; Y describes the proportion of east-facing walls that are facing the sun and for which the road is in sunlight,

$$X = \min(\max(\theta_h - \Theta_0, 0), \pi) - \max(\theta_h - \pi + \Theta_0, 0) - \min(\theta_h + \Theta_0, 0), \tag{43}$$

$$\begin{aligned} Y = {} & \cos\{\max[\min(0, \theta_h), \theta_h - \pi]\} - \cos\{\max[\min(\theta_0, \theta_h), \theta_h - \pi]\} \\ & + \cos\{\min(0, -\theta_h)\} - \cos\{\min(\theta_0, -\theta_h)\} \\ & + \cos\{\max[0, \pi - \theta_h]\} - \cos\{\max[\theta_0, \pi - \theta_h]\}, \end{aligned} \tag{44}$$

where θ_h is related to the solar azimuthal angle by $\theta_h = \pi/2 - \theta_{\mathrm{a}}$. Note that we have still preserved the identity as used in Masson (2000) $S_{\mathrm{in}} = s_{\mathrm{surf},0} + (h/w)(s_{\mathrm{east},0} + s_{\mathrm{west},0})$. The higher order reflections ($i = 1, 2, \ldots, N_r$) are then calculated from

$$s_{\mathrm{surf},i+1} = \alpha_{\mathrm{wall}}(1 - \psi_{\mathrm{surf}})(s_{\mathrm{east},i} + s_{\mathrm{west},i})/2, \tag{45}$$

$$s_{\mathrm{east},i+1} = \alpha_{\mathrm{surf}}\psi_{\mathrm{wall}} s_{\mathrm{road},i} + \alpha_{\mathrm{wall}}(1 - 2\psi_{\mathrm{wall}}) s_{\mathrm{west},i}, \tag{46}$$

where the $s_{\mathrm{west},i+1}$ is calculated in the same way as $s_{\mathrm{east},i+1}$, but with the roles of the east and west walls reversed. α_{surf} is the net albedo of the canyon floor, which also includes the albedo for in-canyon vegetation as determined by

$$\alpha_{\mathrm{surf}} = (1 - \delta_{\mathrm{vegt}})\alpha_{\mathrm{road}} + \delta_{\mathrm{vegt}}\alpha_{\mathrm{vegt}}. \tag{47}$$

Here $\psi_{\mathrm{surf}} = \sqrt{(h/w)^2 + 1} - h/w$ and $\psi_{\mathrm{wall}} = (w/h)[h/w + 1 - \sqrt{(h/w)^2 + 1}]/2$ are the sky-view factors that are defined in Noilhan (1981).

A2. Longwave radiation

Since the emissivity, ϵ, of urban surfaces is relatively close to 1, then many UCMs only calculate first-order reflections for longwave radiation. However, Harman et al. (2004a) found that measurable errors can result in the calculation of longwave radiation if additional reflections were neglected. For completeness, we also calculate the longwave reflections to third order in our UCM (i.e., as used for shortwave radiation). Since the in-canyon vegetation canopy temperature needs to be solved iteratively (see below), as well as potentially an iterative solution for in-canyon snow temperature, then it is useful to precompute longwave reflections in terms of β_* coefficients. For example, the net longwave radiation on each canyon surface is

$$R_{\mathrm{roof}} = \epsilon_{\mathrm{roof}} \left(R_{\mathrm{in}} - \sigma T_{\mathrm{roof}}^4\right), \tag{48}$$

$$R_{\mathrm{road}} = \epsilon_{\mathrm{road}} \left[R_{\mathrm{in}}\beta_{\mathrm{ra}} + R_{\mathrm{surf}}\beta_{\mathrm{rr}} - \sigma T_{\mathrm{road}}^4 + \epsilon_{\mathrm{wall}}\sigma (T_{\mathrm{east}}^4 + T_{\mathrm{west}}^4)\beta_{\mathrm{rw}}\right], \tag{49}$$

$$R_{\mathrm{east}} = \epsilon_{\mathrm{wall}} \left[R_{\mathrm{in}}\beta_{\mathrm{wa}} + (\epsilon_{\mathrm{wall}}\beta_{\mathrm{w0}} - 1)\sigma T_{\mathrm{east}}^4 + \epsilon_{\mathrm{wall}}\sigma T_{\mathrm{west}}^4\beta_{\mathrm{ww}} + R_{\mathrm{surf}}\beta_{\mathrm{wr}}\right], \tag{50}$$

$$R_{\mathrm{vegt}} = \epsilon_{\mathrm{vegt}} \left[R_{\mathrm{in}}\beta_{\mathrm{ra}} + R_{\mathrm{surf}}\beta_{\mathrm{rr}} - \sigma T_{\mathrm{vegt}}^4 + \epsilon_{\mathrm{wall}}\sigma (T_{\mathrm{east}}^4 + T_{\mathrm{west}}^4)\beta_{\mathrm{rw}}\right], \tag{51}$$

where R_{west} is calculated in the same way as for R_{east}, but with the roles of east walls and west walls reversed. σ is the Stefan–Boltzman constant, ϵ_* is the emissivity of $* =$ roof, road, east, west, vegt. The longwave radiation from the canyon floor is modified in the presence of in-canyon vegetation according to

$$R_{\mathrm{surf}} = (1 - \delta_{\mathrm{vegt}})\epsilon_{\mathrm{road}}\sigma T_{\mathrm{road}}^4 + \delta_{\mathrm{vegt}}\epsilon_{\mathrm{vegt}}\sigma T_{\mathrm{vegt}}^4. \tag{52}$$

Outgoing radiation is estimated from

$$\begin{aligned} R_{\mathrm{can}} = {} & \beta_{\mathrm{wa}}\epsilon_{\mathrm{wall}}(h/w)\left[\sigma\left(T_{\mathrm{east}}^4 + T_{\mathrm{west}}^4\right) - 2R_{\mathrm{in}}\right] \\ & + (R_{\mathrm{surf}} - \epsilon_{\mathrm{surf}}R_{\mathrm{in}})\beta_{\mathrm{ra}} + R_{\mathrm{in}}, \end{aligned} \tag{53}$$

where $\epsilon_{\mathrm{surf}} = (1 - \delta_{\mathrm{vegt}})\epsilon_{\mathrm{road}} + \delta_{\mathrm{vegt}}\epsilon_{\mathrm{vegt}}$. The precomputed reflections are determined by the β_* coefficients, which are defined as

$$\beta_* = \sum_{i=1}^{N_{\mathrm{r}}} b_{*,i}, \tag{54}$$

where β_* is reflection coefficient with $* =$ ra, rr, rw, wa, w0, ww, wr (defined below). The incident longwave radiation (zeroth order reflection) is calculated according to the following expressions

$$b_{\mathrm{rr},0} = b_{\mathrm{w}0,0} = 0, \tag{55}$$
$$b_{\mathrm{ra},0} = \psi_{\mathrm{surf}}, \tag{56}$$
$$b_{\mathrm{wa},0} = b_{\mathrm{wr},0} = \psi_{\mathrm{wall}}, \tag{57}$$
$$b_{\mathrm{rw},0} = (1 - \psi_{\mathrm{surf}})/2, \tag{58}$$
$$b_{\mathrm{ww},0} = (1 - 2\psi_{\mathrm{wall}}). \tag{59}$$

The higher order reflections are then calculated from the following recursive relationships

$$b_{\mathrm{ra,i+1}} = (1 - \epsilon_{\mathrm{wall}})(1 - \psi_{\mathrm{surf}})b_{\mathrm{wa,i}}, \tag{60}$$
$$b_{\mathrm{rr,i+1}} = (1 - \epsilon_{\mathrm{wall}})(1 - \psi_{\mathrm{surf}})b_{\mathrm{wr,i}}, \tag{61}$$
$$b_{\mathrm{rw,i+1}} = (1 - \epsilon_{\mathrm{wall}})(1 - \psi_{\mathrm{surf}})(b_{\mathrm{w}0,\mathrm{i}} + b_{\mathrm{ww,i}})/2, \tag{62}$$
$$b_{\mathrm{wa,i+1}} = (1 - \epsilon_{\mathrm{surf}})\psi_{\mathrm{wall}}b_{\mathrm{ra,i}} + (1 - \epsilon_{\mathrm{wall}})(1 - 2\psi_{\mathrm{wall}})b_{\mathrm{wa,i}}, \tag{63}$$
$$b_{\mathrm{w}0,\mathrm{i+1}} = (1 - \epsilon_{\mathrm{surf}})\psi_{\mathrm{wall}}b_{\mathrm{rw,i}} + (1 - \epsilon_{\mathrm{wall}})(1 - 2\psi_{\mathrm{wall}})b_{\mathrm{ww,i}}, \tag{64}$$
$$b_{\mathrm{ww,i+1}} = (1 - \epsilon_{\mathrm{surf}})\psi_{\mathrm{wall}}b_{\mathrm{rw,i}} + (1 - \epsilon_{\mathrm{wall}})(1 - 2\psi_{\mathrm{wall}})b_{\mathrm{w}0,\mathrm{i}}, \tag{65}$$
$$b_{\mathrm{wr,i+1}} = (1 - \epsilon_{\mathrm{surf}})\psi_{\mathrm{wall}}b_{\mathrm{rr,i}} + (1 - \epsilon_{\mathrm{wall}})(1 - 2\psi_{\mathrm{wall}})b_{\mathrm{wr,i}}. \tag{66}$$

In practice, the β_* coefficients are calculated at the start of each timestep, while the urban canyon temperatures for T_{road}, T_{east}, T_{west} and T_{vegt} can be updated later in the UCM. This means that it is possible to solve for T_{vegt} (and potentially T_{roadsnow}) using an iterative approach without having to re-calculate R_{vegt} for each iteration.

A3. Canyon and roof fluxes

Following TEB, we divide the urban scheme into contributions from the building roofs and from the urban canyon (i.e., combining contributions from canyon walls, roads and vegetation as described in Eq. 4). The sensible heat flux from the canyon and from the roofs can then be written as

$$H_{\mathrm{can}} = \rho_{\mathrm{a}} C_{\mathrm{a}} (T_{\mathrm{can}} - T_{\mathrm{atmc}}) / \Omega_{\mathrm{can}}, \tag{67}$$
$$H_{\mathrm{roof}} = \rho_{\mathrm{a}} C_{\mathrm{a}} \left(T_{\mathrm{roof}} - T_{\mathrm{atmr}}\right) / \Omega_{\mathrm{roof}}, \tag{68}$$

where Ω_{roof} is the aerodynamic resistance between the roof surfaces and the atmosphere, whereas Ω_{can} is the aerodynamic resistance between the canyon displacement height and the atmosphere; T_{atmc} is the temperature of the lowest model level reduced to the canyon displacement height and T_{atmr} is the equivalent temperature of the lowest atmospheric level after being reduced to the roof height using the Exner function (see, for example, Masson 2000); T_{can} is a diagnosed temperature for the canyon which satisfies Eq. 4. We can also write the latent heat fluxes for the canyon and roof tiles as

$$LE_{\mathrm{can}} = \rho_{\mathrm{a}} L_{\mathrm{v}} (q_{\mathrm{can}} - q_{\mathrm{atmc}}) / \Omega_{\mathrm{can}}, \tag{69}$$
$$LE_{\mathrm{roof}} = w_{\mathrm{roof}} \rho_{\mathrm{a}} L_{\mathrm{v}} \left(\mathrm{qsat}_{\mathrm{roof}} - q_{\mathrm{atmr}}\right) / \Omega_{\mathrm{roof}}, \tag{70}$$

where L_{v} is the latent heat of vaporization, $\mathrm{qsat}_{\mathrm{roof}}$ is the saturated mixing ratio for the roof, q_{atmr} is the equivalent mixing ratio for the lowest atmospheric level after being reduced to the roof height and q_{atmc} is the mixing ratio of the lowest atmospheric level reduced to the canyon displacement height. q_{can} is a diagnosed mixing ratio that satisfies Eq. 5 and w_{roof} denotes the fraction of roofs that is covered by water and is defined below.

Note that, although most UCMs use MOST for coupling the roof tile to the atmosphere with the roof roughness length, $z_{0,\mathrm{roof}}$, there is a variety of methods for calculating the aero-

dynamic resistance between the atmosphere and the canyon. A turbulent kinetic energy based approach has been used in Martilli et al. (2002), whereas separate coupling for the venting and recirculation regions was used in Harman et al. (2004b) based on the resistant transport across the shear layer. In this paper we have followed the approach of Masson (2000) and simply assumed classical surface boundary-layer laws using the urban roughness length, $z_{0,urb}$ and stability functions from Dyer and Hicks (1970). Estimating the roughness length for heat for urban areas has been discussed by Voogt and Grimmond (2000) and Kanda et al. (2007). The results of Kanda et al. (2007) suggest that a canyon roughness length for heat, $z_{T,\mathrm{can}}$, at approximately 10% of the building height is reasonable for calculating Ω_{can}, when the air temperature is used for the canyon temperature (i.e., T_{can}). When calculating screen level temperature and the 10-m wind speed for the urban area, we assume the roughness length for heat, $z_{T,\mathrm{urbn}}$, can be estimated from the theoretical bluff-rough formulation used in Voogt and Grimmond (2000) and Kanda et al. (2007).

A4. Conduction

As used for TEB, our UCM employs three layers for building roofs, roads and walls to represent the conduction of heat through building materials. The expression for the conduction of heat is (see Masson 2000)

$$G_{*,i} = \frac{2(T_{*,i} - T_{*,i+1})}{d_{*,i}/\lambda_{*,i} + d_{*,i+1}/\lambda_{*,i+1}}, \tag{71}$$

where $^* =$ roof, road, east, west, $d_{*,i}$ is the thickness of the ith layer and $\lambda_{*,i}$ is the conduction of the ith layer. The boundary condition third layer of the roof or wall surfaces is determined by the interior building temperature T_{bld}, while the third layer of the road surface has a zero flux boundary condition.

A5. Surface water

Following Masson (2000), we use a bucket model approach to describe the water on roof and road surfaces, i.e.,

$$\frac{\mathrm{d}W_*}{\mathrm{d}t} = Rnd - LE_*/L_{\mathrm{v}}, \tag{72}$$

where $^* =$ roof, road. The maximum value of W_{roof} and W_{road} is limited to $0.1\,\mathrm{kg\,m^{-2}}$, with the excess water removed by drainage. The water cover on these surfaces, w_* is calculated using the expression from Masson (2000), where $w_* = (W_*/\max W_*)^{2/3}$.

A6. Model parameters

A possible weakness of many UCMs is their use of a large number of parameters. For this study we attempt to constrain the UCM parameters to agree with field measurements of Coutts et al. (2007) and building material properties derived from Masson et al. (2003). Tables 4 and 5 define the UCM parameters, with Table 4 describing urban composition properties and Table 5 describing building material properties and some vegetation parameters. Note that we have also indicated the origin of the parameter in the tables.

The roof thickness has been modified from that suggested in Masson et al. (2003) to help improve the simulated minimum temperature. We have also used a 4 m depth of soil instead of a 1 m soil depth to improve the seasonal cycle of road temperatures. Note that the vegetation area fraction, δ_{veg}, agrees with the value from Coutts et al. (2007) when multiplied

Table 4 Urban composition parameters used by the UCM

Parameter	Value	Source
δ_{bld}	0.45	Coutts et al. (2007)
δ_{veg}	0.69	Coutts et al. (2007)
h	6 m	Coutts et al. (2007)
h/w	0.4	Coutts et al. (2007)
T_{bld}	291 K	Masson (2000)
H_{traf}	3 W m^{-2}	Coutts et al. (2007)
LAI	3	
m_{swilt}	0.18	Kowalczyk et al. (1994)
m_{sfc}	0.26	Kowalczyk et al. (1994)
c_1	1.478	Kowalczyk et al. (1994)
$z_{0,\text{urbn}}$	0.6 m	Masson et al. (2003)
$z_{0,\text{roof}}$	0.01 m	
$z_{0,\text{road}}$	0.01 m	
$z_{0,\text{wall}}$	0.01 m	
$z_{0,\text{veg}}$	0.1 m	

Table 5 Urban building material parameters used by the UCM

Parameter	Roof	Wall	Road	Vegt	Source
Albedo	0.20	0.30	0.10	0.20	Fortuniak (2008)
Emissivity	0.90	0.85	0.94	0.96	Masson et al. (2003)
					Lee and Park (2008)
Thickness 1 (m)	0.10	0.05	0.05		Masson et al. (2003)
Thickness 2 (m)	0.40	0.10	0.10		Masson et al. (2003)
Thickness 3 (m)	0.10	0.05	4.00		Masson et al. (2003)
Heat capacity 1 (J m^{-3} K^{-1})	2.11×10^6	1.55×10^6	1.94×10^6		Masson et al. (2003)
Heat capacity 2 (J m^{-3} K^{-1})	0.28×10^6	1.55×10^6	1.28×10^6		Masson et al. (2003)
Heat capacity 3 (J m^{-3} K^{-1})	0.29×10^6	0.29×10^6	1.28×10^6		Masson et al. (2003)
Conductance 1 (W m^{-1} K^{-1})	1.51	0.94	0.75		Masson et al. (2003)
Conductance 2 (W m^{-1} K^{-1})	0.08	0.94	0.25		Masson et al. (2003)
Conductance 3 (W m^{-1} K^{-1})	0.05	0.05	0.25		Masson et al. (2003)

by $(1 - \delta_{\text{bld}})$. The roughness length for the urban area is based on the usual approximation which is 10% of the building height.

References

Coutts A, Beringer J, Tapper N (2007) Impact of increasing urban density on local climate: Spatial and temporal variations in the surface energy balance in Melbourne, Australia. J Appl Meteorol 46:477–493

Davies H (1976) A lateral boundary formulation for multi-level prediction models. Q J Roy Meteorol Soc 102:405–418

Douville H, Royer JF, Mahfouf JF (1995) A new snow parameterization for the meteo-france climate model—part I: validation in stand-alone experiments. Clim Dyn 12:21–35
Dyer A, Hicks B (1970) Flux–gradient relationships in the constant flux layer. Q J Roy Meteorol Soc 96: 715–721
Fortuniak K (2008) Numerical estimation of the effective albedo of an urban canyon. Theor Appl Climatol 91:245–258
Harman I, Belcher S (2006) The surface energy balance and boundary layer over urban street canyons. Q J Roy Meteorol Soc 132:2749–2768
Harman I, Barlow J, Belcher S (2004a) Scalar fluxes from urban street canyons. Part II: model. Boundary-Layer Meteorol 113:387–409
Harman IN, Best MJ, Belcher SE (2004b) Radiative exchange in an urban street canyon. Boundary-Layer Meteorol 110:301–316
Hurley P (2007) Modelling mean and turbulence fields in the dry convective boundary layer with the eddy-diffusivity/mass-flux approach. Boundary-Layer Meteorol 125:525–526
Hurley P, Luhar A (2009) Modelling the meteorology at the Cabauw Tower for 2005. Boundary-Layer Meteorol 132:43–57
Hurley P, Physick W, Luhar A (2005) TAPM—a practical approach to prognostic meteorological and air pollution modelling. Environ Model Softw 20:737–752
Jacob DJ, Winner DA (2009) Effect of climate change on air quality. Atmos Environ 43:51–63
Kanda M, Kawai T, Kanega M, Moriwaki R, Narita K, Hagishima A (2005) A simple energy balance model for regular building arrays. Boundary-Layer Meteorol 116:423–443
Kanda M, Kanega M, Kawai T, Moriwaki R (2007) Roughness lengths for momentum and heat derived from outdoor urban scale models. J Appl Meteorol 46:1067–1079
Kowalczyk EA, Garratt JR, Krummel PB (1994) Implementation of a soil-canopy scheme into the CSIRO GCM—regional aspects of the model response. CSIRO Division of Atmospheric Research Technical Paper 32, 65 pp
Kusaka H, Kondo H, Kikegawa Y, Kimura F (2001) A simple single-layer urban canopy model for atmospheric models: comparison with multi-layer and slab models. Boundary-Layer Meteorol 101:329–358
Lee SH, Park SU (2008) A vegetated urban canopy model for meteorological and environmental modelling. Boundary-Layer Meteorol 126:73–102
Martilli A, Clappier A, Rotach M (2002) An urban surface exchange parameterisation for mesoscale models. Boundary-Layer Meteorol 104:261–304
Masson V (2000) A physically-based scheme for the urban energy budget in atmospheric models. Boundary-Layer Meteorol 94:357–397
Masson V, Champeaux JL, Chauvin F, Meriguet C, Lacaze R (2003) A global database of land surface parameters at 1-km resolution in meteorological and climate models. J Clim 16:1261–1282
Noilhan J (1981) A model for the net total radiation flux at the surface of a building. Build Environ 16:259–266
Ohashi Y, Genchi Y, Kondo H, Kikegawa Y, Yoshikado H, Hirano Y (2007) Influence of air-conditioning waste heat on air temperature in Tokyo during summer: numerical experiments using an urban canopy model coupled with a building energy model. J Appl Meteorol 46:66–81
Oke TR (1988) The urban energy balance. Prog Phys Geogr 12:471–508
Sailor DJ (2001) Relating residential and commercial sector electricity loads to climate-evaluating state level sensitivities and vulnerabilities. Energy 26:645–657
Voogt J, Grimmond C (2000) Modelling surface sensible heat flux using surface radiative temperatures in a simple urban area. J Appl Meteorol 39:1679–1699